

456  
457  
458  
459  
460  
461  
462  
463  
464  
465  
466  
467  
468  
469  
470  
471  
472  
473  
474  
475  
476

## Supplementary Information

### A glycan gate controls opening of the SARS-CoV-2 spike protein

Terra Sztain<sup>1†</sup>, Surl-Hee Ahn<sup>1†</sup>, Anthony T. Bogetti<sup>2</sup>, Lorenzo Casalino<sup>1</sup>, Jory A. Goldsmith<sup>3</sup>,  
Evan Seitz<sup>4</sup>, Ryan S. McCool<sup>3</sup>, Fiona L. Kearns<sup>1</sup>, Francisco Acosta-Reyes<sup>5</sup>, Suvrajit Maji<sup>5</sup>,  
Ghoncheh Mashayekhi<sup>6</sup>, J. Andrew McCammon<sup>1,7</sup>, Abbas Ourmazd<sup>6</sup>, Joachim Frank<sup>4,5</sup>, Jason S.  
McLellan<sup>3</sup>, Lillian T. Chong<sup>2\*</sup>, Rommie E. Amaro<sup>1\*</sup>

1. Department of Chemistry and Biochemistry, UC San Diego, La Jolla, CA 92093
2. Department of Chemistry, University of Pittsburgh, Pittsburgh, PA 15260
3. Department of Molecular Biosciences, The University of Texas at Austin, Austin, TX 78712
4. Department of Biological Sciences, Columbia University, New York, NY, 10032, USA
5. Department of Biochemistry and Molecular Biophysics, Columbia University Medical Center, New York, NY 10032, USA
6. Department of Physics, University of Wisconsin-Milwaukee, 3135 N. Maryland Ave, Milwaukee, WI 53211, USA
7. Department of Pharmacology, UC San Diego, La Jolla, CA 92093

† These authors contributed equally to this work.

\* contact authors: [ramaro@ucsd.edu](mailto:ramaro@ucsd.edu), [ltchong@pitt.edu](mailto:ltchong@pitt.edu)

477	<b>Table of Contents</b>
478	<b>1. Supplementary Methods</b>
479	<b>1.1 Computational Methods</b>
480	<b>1.1.1</b> Model preparation of the initial “down” state
481	<b>1.1.2</b> Weighted ensemble simulations
482	<b>1.1.3</b> Analysis of weighted ensemble simulations
483	<b>1.2 ManifoldEM Methods</b>
484	<b>1.2.1</b> Background
485	<b>1.2.2</b> Preprocessing
486	<b>1.2.3</b> Manifold embedding
487	<b>1.2.4</b> Comparison of WE simulations to manifold outputs
488	<b>1.3 Experimental Methods</b>
489	<b>2. Supplementary Figures 1 – 16</b>
490	<b>3. Supplementary Tables 1 – 2</b>
491	<b>4. Supplementary Videos 1 – 5</b>
492	<b>5. Supplementary References</b>
493	
494	
495	
496	
497	
498	
499	
500	

## 501 1. Supplementary Methods

502

### 503 1.1 Computational Methods

504

#### 505 1.1.1 Model preparation of the initial “down” state

506 A model of the “down” state of the glycosylated spike structure and CHARMM36 force field  
507 parameters<sup>31,32</sup> was obtained from Casalino *et al.*,<sup>8</sup> modeled using the cryoEM structure (PDB ID:  
508 6VXX);<sup>5</sup> in this model hydrogen atoms were added using ionization states present in solution at  
509 pH 7.4. The stalk and membrane were excluded, and only residues 16-1140 of each trimer were  
510 used (**Fig. 1A**). The system was solvated in a cubic box of TIP3P<sup>33</sup> explicit water molecules with  
511 at least 10 Å between the protein and box edges and 150 mM NaCl using VMD,<sup>34</sup> yielding a  
512 system size of 490,621 atoms. The GPU-accelerated Amber18<sup>35,36,37,38</sup> molecular dynamics (MD)  
513 engine was used, which gave a 16-fold speedup in dynamics propagation on a GPU vs. CPU. To  
514 enable the use of the Amber18 software package, the Chamber program<sup>39</sup> was used to convert  
515 the CHARMM36 force field parameters into an Amber readable format.

516

517 To relieve unfavorable interactions, the solvated system was subjected to a two-stage energy  
518 minimization followed by a two-stage equilibration. To minimize the energy of the system, the  
519 solvent was first minimized for 10,000 steps with harmonic position restraints (force constant of  
520 100 kcal/mol /Å<sup>2</sup>) applied to the sugars and proteins followed by an unrestrained minimization of  
521 the entire system for 100,000 steps. To equilibrate the energy-minimized system, the system was  
522 incrementally heated to 300 K over 300 ps in the NVT ensemble followed by a 1-ns equilibration  
523 in the NPT ensemble. A production simulation was then carried out in the NPT ensemble for 20  
524 ns on the Triton Shared Computing Cluster at San Diego Supercomputer Center (SDSC).

525 Equilibration and production simulations were carried out with a 2 fs timesteps and SHAKE<sup>40</sup>  
526 constraints on bonds to hydrogens. Pressure and temperature were controlled with the Monte  
527 Carlo barostat (with 100 fs between attempts to adjust the system volume) and the Langevin  
528 thermostat (1 ps<sup>-1</sup> collision frequency), respectively. Long-range electrostatics were accounted  
529 for with the PME method<sup>41</sup> using a 10 Å cutoff for short-range, non-bonded interactions. To  
530 provide more extensive sampling of the closed state, we selected a set of 24 equally weighted  
531 conformations (“basis states”) from the latter 5 ns of the production simulation for a weighted

532 ensemble (WE) simulation; this portion of the simulation exhibited reasonable convergence of  
533 the C $\alpha$  root-mean-squared deviation (RMSD) from the initial, minimized conformation  
534 (**Supplemental Fig. 6**).

535

### 536 **1.1.2 Weighted ensemble simulations**

537 The weighted ensemble (WE) path sampling strategy orchestrates an ensemble of parallel  
538 trajectories with periodic communication to enhance the sampling of pathways for rare events  
539 without biasing the dynamics.<sup>15</sup> In particular, a resampling step is applied at fixed time intervals  
540  $\tau$  to enrich for promising trajectories that have advanced towards the target state – typically,  
541 along a progress coordinate that has been divided into bins. Trajectories are all initially assigned  
542 equal statistical weights and rigorously tracked to ensure that all weights sum to one at all times  
543 of the simulation, introducing no bias in the dynamics.<sup>12</sup> During the resampling step, trajectories  
544 that transition to empty bins are replicated and their corresponding weights split evenly between  
545 the resulting child trajectories; trajectories that do not make progress are occasionally  
546 terminated with their respective weights merged to other trajectories that will be  
547 continued. (**Supplemental Fig. 1**)

548

549 WE simulations can be run under non-equilibrium steady state or equilibrium conditions and can  
550 therefore provide equilibrium (*e.g.*, state populations) and non-equilibrium observables (*e.g.*, rate  
551 constants), respectively. To maintain non-equilibrium steady-state conditions, trajectories that  
552 reach the target state are “recycled” by initiating a new trajectory from the initial state with the  
553 same trajectory weight; steady-state WE simulations therefore require that the target state be  
554 defined in advance of the simulation, but are more efficient in generating successful events than  
555 equilibrium WE simulations. On the other hand, equilibrium WE simulations do not require a  
556 fixed definition of the target state and therefore enable refinement of the target-state definition at  
557 any time during the simulation. Here, we leveraged the advantages of both non-equilibrium  
558 steady state and equilibrium WE simulations: steady-state simulations were used to more  
559 efficiently generate successful pathways trajectories once the target state could be defined and  
560 equilibrium simulations were used to further explore and refine the definition of the target state.

561

562 All WE simulations were run using the open-source, highly scalable WESTPA software  
563 package<sup>42</sup> (**Supplemental Fig. 7**) with a fixed time interval  $\tau$  of 100 ps for resampling and a  
564 target number of 8 trajectories/bin. Details of the progress coordinate and bin spacing for each  
565 WE simulation are provided below.

#### 567 *Extensive sampling of the initial “down” state*

568 To extensively sample the initial “down” state, we ran an equilibrium WE simulation starting  
569 from randomly selected conformations from the basis states discussed above. A two-dimensional  
570 progress coordinate was used. One dimension consisted of the distance between the centers of  
571 mass (COM) of (i) C $\alpha$  atoms of the entire system **and** all atoms in the four main beta strands of  
572 the RBD (residues 375-380, 394-404, 431-438, 508-517; refers to RBD from chain A unless  
573 otherwise specified), and (ii) C $\alpha$  atoms of the entire system **and** all atoms in the structured region  
574 of the helical core domain (residues 747-784, 946-967, 986-1034 from each of the three chains).  
575 The second dimension consisted of the C $\alpha$  RMSD of the entire system and all atoms in the four  
576 main beta strands of the RBD from the initial model of the “down”-state structure after 1 ns  
577 equilibration. Progress coordinates were calculated using CPPTRAJ.<sup>43</sup> This initial WE  
578 simulation was run for 8.77 days on 80 P100 GPUs on Comet at the San Diego Supercomputer  
579 Center (SDSC) collecting a comprehensive sampling of  $\sim 7.5 \mu\text{s}$  aggregate simulation time. Bin  
580 spacing was periodically monitored and adjusted to maximize efficient sampling.

581  
582 Due to a typo in the CPPTRAJ atom selection (*i.e.*, “and” instead of “of”), the progress  
583 coordinate above was not the one we originally intended. Our intention was to use 1) the COM  
584 distance between the C $\alpha$  atoms **of** the four main beta sheets of the RBD and the C $\alpha$  atoms of the  
585 structured region of the helical core domain and 2) the C $\alpha$  RMSD **of** the four main beta sheets of  
586 the RBD from the initial model of the “down”-state structure. As shown in **Figs. 2F and S2**, our  
587 WE simulations with this progress coordinate nonetheless capture the large-scale protein  
588 transitions that are evident with the intended progress coordinate, but on a more compressed  
589 scale.

590

#### 591 *Simulations of spike opening*

592 After extensive sampling of the “down” state, exploratory WE simulations were run to determine  
593 effective progress coordinates and binning to capture the opening of the spike protein. Based on  
594 these simulations, we found that taking the RMSD from the target “up” state was much more  
595 effective than taking the RMSD from the initial “down” state. The target state, with one RBD in  
596 the “up” conformation, modeled by Casalino *et al.*<sup>8</sup> using the cryoEM structure (PDB ID:  
597 6VSB),<sup>4</sup> was subject to 1 ns of equilibration using identical methods as described above for the  
598 closed structure. The RMSD of the initial state from the target state was calculated as 11.5 Å.

599  
600 Next, an independent, equilibrium WE simulation was conducted using the two-dimensional  
601 progress coordinate described above for sampling the “down” state, but taking the RMSD from  
602 the target “up” state instead of the initial “down” state and using the bin spacing determined by  
603 the exploratory simulations. The WE simulation was stopped for analysis after 1729 iterations,  
604 19.64 days on 100 NVIDIA V100 GPUs on Longhorn at TACC, collecting an aggregate of ~51.5  
605 μs of sampling and 106 pathways from the “down” to the “open” state. Finally, another WE  
606 simulation that was under non-equilibrium steady-state conditions was conducted to maximize  
607 sampling of transitions from the “down” to the “up” states. This WE simulation started from  
608 iteration 1576 of the previous WE simulation, which was the last iteration before the RBD-COM  
609 distance was 9.0 Å or greater, was stopped for analysis after 3000 iterations, 25.03 days later, on  
610 100 NVIDIA V100 GPUs on Longhorn at TACC, collecting an additional ~69.2 μs of sampling  
611 and 204 pathways from the “down” to the “open” state. The WESTPA software was shown to  
612 scale almost linearly on these 100 NVIDIA V100 GPUs on Longhorn (**Supplemental Fig. 7**),  
613 which enabled fast and efficient simulation of the spike.

614

### 615 **1.1.3 Analysis of weighted ensemble simulations**

#### 616 *Number of successful pathways*

617 The successful pathways that reached the “up” state ( $8.9 \text{ \AA} \leq \text{RBD-COM distance}$ ) or the “open”  
618 state ( $9.9 \text{ \AA} \leq \text{RBD-COM distance}$ ) were obtained by counting all arrivals to that particular state  
619 at every WE iteration, which yielded 204 and 106 pathways, respectively. We consider these  
620 pathways to be statistically independent pathways. The splitting trees for the 204 and 106  
621 pathways, respectively, can be seen in **Supplemental Figs. 8 and 9**, respectively, which shows  
622 trajectory segments shared by the pathways and points of splitting the pathways. The number of

623 pathways is similar to that obtained from calculating the autocorrelation function of arrivals to  
624 the “up” and “open” states at a particular WE iteration. For instance, at the end of the WE  
625 simulation that sampled the “open” state, there were 1824 trajectories in total and 1193  
626 trajectories that were part of the “open”-state ensemble (defined in later sections as  $9.0 \text{ \AA} \leq$   
627 RBD-COM distance). Out of the 1193 trajectories that reached the “open”-state ensemble, 133  
628 trajectories were calculated to be statistically independent from calculating the autocorrelation  
629 function of the number of arrivals to the “open”-state ensemble<sup>19</sup> (**Supplemental Fig. 10**). The  
630 correlation time was calculated to be 16 WE iterations or 1.6 ns so the trajectories that did not  
631 share a common segment for 16 iterations from the last point in the trajectory were considered to  
632 be statistically independent. By checking these multiple independent pathways that reached the  
633 “up” or “open” states, we were able to confirm reproducibility of the identified glycan and  
634 residue interactions involved in the particular transition. For calculating the shortest and longest  
635 transition times, all successful pathways were taken into account. The first 25% of all successful  
636 pathways were disregarded to obtain the most probable transition times, however, since the  
637 initial transitions can skew the transition time to be shorter than it is normally (**Supplemental**  
638 **Figs. 11 and 12**).

639

#### 640 *State definitions*

641 Based on our WE simulations, key states were defined as follows. The “down”-state ensemble  
642 consisted of structures with  $\text{RMSD} \geq 11.0 \text{ \AA}$  and RBD-COM distance  $\leq 7.5 \text{ \AA}$ ,  $\sim 13 \mu\text{s}$  aggregate  
643 simulation time. Note that the entire progress coordinate array had to satisfy the criteria to be  
644 counted as part of the ensemble. The “up”-state ensemble was defined as  $8.5 \text{ \AA} \leq$  RBD-COM  
645 distance  $< 9.0 \text{ \AA}$ ,  $\sim 6.5 \mu\text{s}$  aggregate simulation time. The “open”-state ensemble was defined as  
646 having an RBD-COM distance  $\geq 9.0 \text{ \AA}$ ,  $\sim 4.9 \mu\text{s}$  aggregate simulation time.

647

#### 648 *Trajectory analysis*

649 Trajectories were visualized using VMD.<sup>34</sup> Glycans, salt bridge, and hydrogen bonding  
650 interactions involved in the “down” to “up” and “open” transition were first visually identified.  
651 Next, distances between the identified residues were calculated using `cpptraj`<sup>43</sup> for all 310  
652 successful pathways, and plotted with `matplotlib`.<sup>44</sup> To obtain the percentage of the most  
653 probable transition time that had a certain salt bridge, the distance between the atoms/residues of

654 the salt bridge was measured, and the total time in which the distance was less than 3.5 Å was  
655 calculated. The total time for each pathway was calculated and averaged to obtain the final  
656 percentage. To obtain the number of successful pathways that had a certain quantity, *e.g.*, salt  
657 bridge, glycan-residue contact, the pathway was counted if the distance was less than 3.5 Å in at  
658 least one of the conformations, sampling conformations every 100 ps. Contact maps calculating  
659 the distance between the RBD (from chain A) and all other residues and glycans were generated  
660 using MDAnalysis<sup>45,46</sup> (**Supplemental Video 5**). Structures for figures and movies were  
661 generated using VMD, including NanoShaper<sup>47</sup> surface representation.

662  
663 Solvent accessible surface area (SASA) was calculated using a protocol presented in Casalino *et*  
664 *al.*<sup>8</sup> involving the *measure\_sasa* command within VMD and a solvent probe radius of 1.4 Å. The  
665 surface area of the Receptor Binding Motif (RBM, residues 438-508 in chain A) that was  
666 shielded by glycans was calculated by taking the difference between the SASA of the “naked”  
667 spike (without glycans) and the SASA of the glycosylated spike (with glycans). Individual  
668 contributions to shielding of the RBM by glycans at positions N165-B, N234-B, N343-B were  
669 also calculated by considering only the respective glycans in the SASA calculation of the  
670 glycosylated spike.

671  
672 *Analysis of residues mutated in emerging SARS-CoV-2 strains*

673 To date, the following SARS-CoV-2 variants have been identified (with mutations to spike noted  
674 in parentheses): B.1 (D614G), B.1.1.7 (H69-V70 deletion, Y144-Y145 deletions, N501Y,  
675 A570D, D614G, P681H, T716I, S982A, D1118H), B.1.351: (L18F, D80A, D215G, R246I,  
676 K417N, E484K, N501Y, D614G, A701V), P1 (L18F, T20N, P26S, D138Y, R190S, K417T,  
677 E484K, N501Y, D614G, H655Y, T1027I) and CAL.20C (L452R, D614G).<sup>28</sup> To examine  
678 potential implications of these mutations on Spike opening mechanics, we have monitored the  
679 neighboring residues of key WT residues as a function of the opening mechanism.

680 MDAnalysis<sup>45,46</sup> was used to identify residues whose center of mass was within 10 Å of the  
681 center of mass of the key residue of interest. For each contact, the fraction of conformations in  
682 the “down”, “up”, and “open” ensembles containing the contact is provided. Contacts were only  
683 considered if they exist within > 5% of all conformations and if the contacting pairs were  
684 separated by more than three peptide bonds in one-dimensional sequence.



685

## 686 **1.2 ManifoldEM method**

687

### 688 **1.2.1 Background**

689 The set of algorithms now under the name ManifoldEM<sup>48</sup> employ a three-step procedure<sup>22</sup> to  
690 characterize conformational variations in a dataset from single-particle cryo-EM of a molecule in  
691 thermal equilibrium. In the first step, which can be performed on any of the existing cryo-EM  
692 platforms, data are classified by orientation, and prepared as aligned image stacks. In the second  
693 step, for each projection direction (PD) data falling into the angular aperture are analyzed as a  
694 manifold and represented in a low-dimensional space spanned by what is now termed  
695 “conformational coordinates,”<sup>48</sup> equivalent to collective motion coordinates. In the third step,  
696 the manifold representations resulting from the second step, one for each projection direction, are  
697 reconciled and combined across the angular sphere to obtain a consolidated representation. From  
698 this an energy landscape can be obtained, enabling a functional analysis of the molecule,<sup>48</sup> and  
699 3D volumes can be captured along inferred trajectories.

700

### 701 **1.2.2 Preprocessing**

702 The initial image-stack we received from McLellan and colleagues corresponding to PDB ID:  
703 6VSB<sup>4</sup> contained 631,920 snapshots. This initial image stack was pruned by approximately 10%  
704 (from 631,920 to 578,588 particles) to remove artifacts. Additional 3D Auto-Refinement via  
705 RELION<sup>49</sup> was performed to realign all images. Next RELION 2D Classification was used to  
706 remove an additional 1% of particles, leaving the final count of 574,324. The consensus  
707 refinement in RELION displayed a Fourier Shell Correlation ( $FSC_{0.143}$ ) of 4.3 Å. In parallel, this  
708 stack was separately refined using CryoSPARC<sup>50</sup> non-uniform refinement with a GSFSC  
709 resolution of 3.5 Å.

710

711 These two refinements were next compared within the preliminary steps of ManifoldEM.  
712 Although both reconstructions appeared fine, we found upon closer examination that the  
713 RELION refinement encountered a problem of preferred orientations, where thousands of  
714 particles had been clumped within nearly the same local area (*i.e.*, nearly identical Euler  
715 coordinates) of the 2-sphere. In contrast, the CryoSPARC non-uniform refinement produced

716 much more uniformly-distributed angular assignments, albeit with a lower average occupancy  
717 per PD. 2D conformational coordinate movies obtained in ManifoldEM from the CryoSPARC  
718 alignment proved superior to those using RELION. While the CryoSPARC alignment was  
719 chosen for all subsequent steps in ManifoldEM, the RELION protocol was not altogether without  
720 its own merit. We additionally ran RELION focused 3D Classification using the angular  
721 alignment from CryoSPARC with a mask around the RBDs. We obtained classes with different  
722 configurations of the RBD, including one class in the RBD-“down” conformation  
723 (**Supplemental Fig. 4**). The original study,<sup>4</sup> in contrast, found no such particles - nor did other  
724 labs to which the data were sent for further analysis. Importantly, the discovery of these missing  
725 particles explains the presence of RBD-“down” volumes constructed along the 3DVA<sup>51</sup> “reaction  
726 coordinate” discovered in that study.<sup>4</sup>

727

### 728 **1.2.3 Manifold embedding**

729 We next set up a more thorough ManifoldEM analysis using the cryoSPARC alignment. First, a  
730 number of initial inputs are required for the ManifoldEM pipeline to tessellate the orientational  
731 2-sphere into a finite number of PDs. These are (1) Pixel size: 1.047 Å; (2) Resolution: 3.5 Å; (3)  
732 Object diameter: 335 Å (taken as the maximum width of the average volume); and (4) Aperture  
733 index: {1-5}. The aperture index is a flexible parameter that controls the angular width of each  
734 PD, such that a larger aperture index corresponds to more images assigned to each PD from a  
735 larger region of angular space. After experimenting with several aperture indices and evaluating  
736 the corresponding PD statistics and 2D movie qualities, we chose aperture index 5 for all future  
737 computations. This measure provided us with 1678 PDs thoroughly spread out in angular space,  
738 with a handful of regions with heightened PD-occupancy. When displayed as a histogram, the  
739 occupancy of PDs exhibited a chi-squared distribution, with the majority of PDs housing around  
740 230 images and a rightward tail reaching approximately 800 images in the most highly-occupied  
741 PD.

742

743 Following the ManifoldEM framework, 1678 manifolds were constructed from the images in  
744 each corresponding PD via the Diffusion Maps<sup>52</sup> framework. Following Dashti et al.,<sup>22</sup>  
745 Nonlinear Laplacian Spectral Analysis (NLSA)<sup>53</sup> was then performed on the eigenvectors of  
746 these high-dimensional manifolds to extract a set of possible reaction coordinates from each. In

747 sum, these steps were programmed to produce eight 2D movies per PD, with each 2D movie  
748 corresponding to one of the PD-manifold's eigenvectors.

749

### 750 *Conformational analysis*

751 Upon completion, our task was to next classify the type of motions seen in each 2D movie per  
752 PD, noting that not all 2D movies extracted must correspond to valid conformational  
753 information; this is especially true of those obtained with smaller singular values. Our approach  
754 was to initiate a search to detect all PDs housing 2D movies with above-average visual  
755 appearance. In this search, many PD-manifolds were found to have extremely noisy or otherwise  
756 insensible information. This was a predictable scenario given the known deficiencies in the  
757 dataset<sup>4</sup> (*i.e.*, orientational bias leading to low occupancies in many PDs), and beyond  
758 remediation by ManifoldEM. As a result, only a subset of PDs where the images therein met the  
759 prerequisites for the manifold embedding approach could be analyzed. Of these above-threshold  
760 PDs, we found 216 PDs of the 1678 PDs (13%) with above average quality and 73 high-quality  
761 PDs (4%), as judged by visual inspection relative to the whole. Thus, overall, a relatively small  
762 percentage of the data as partitioned into these PDs met the prerequisite conditions for displaying  
763 the highest-quality conformational variation signals.

764

765 We next organized all above-average PDs into 22 well-spaced groups on the 2-sphere, and  
766 selected several of the best PDs from each angular region. Detailed analysis was performed on  
767 the 64 PDs chosen, including classification of conformational motion type in each of the eight  
768 2D NLSA movies per PD. As shown in **Supplementary Videos 2 and 3**, we predominantly  
769 observed two conformational motions: (1) RBD-“down” to RBD-“up”; and (2) trimer-claw close  
770 to open, which we call conformational coordinate 1 (CC1) and conformational coordinate 2  
771 (CC2), respectively. However, PDs where a clear distinction existed between CC1 and CC2 were  
772 rare. Specifically, CC1 alone could only be clearly established in 31 of 64 PDs (48%); while both  
773 CC1 and CC2 were found occupying separate 2D movies in only 6 of 64 PDs (9%). In the  
774 remaining PDs, these conformational motions were not cleanly separated but were present in  
775 hybrid form.

776

777 This discrepancy arises from the nature of our analysis, where we define Euclidean distances  
778 between images that are 2D projections of the molecule. As a result, from a given viewing  
779 direction, a 3D motion projected onto 2D will appear more or less pronounced than it does in  
780 some other, depending on the type of motion and PD. For example, we found that the CC2 trimer  
781 claw motion was most pronounced only when observed from the “top-down view”, the PD  
782 aligned with the axis of the protein’s central alpha helices (PD 112).

783

784

#### 785 *Transformation of structures along WE trajectory*

786 We next aimed to compare the conformational coordinates discovered by ManifoldEM from  
787 experimental cryo-EM ensembles with the WE motions observed in the spike-opening trajectory  
788 detailed in the main text. To this end, we converted the PDB files from the WE into a collection  
789 of 2D projections. We first selected 20 frames from the WE trajectory spanning conformations  
790 from the RBD-“down” to the RBD-“up” state. We next imported these files into Chimera<sup>54</sup> along  
791 with a coarse 3D map obtained from ManifoldEM to be used for alignment reference. In order to  
792 place both frameworks in the same coordinate system for subsequent analysis, we translated and  
793 rotated the PDB files to coincide with the ManifoldEM map, using the Chimera fitmap  
794 command. Each PDB was then saved in Chimera. Next, these fitted PDBs were re-centered using  
795 Phenix<sup>55</sup> pdbtools and converted into MRC-formatted Coulomb potential maps via EMAN2<sup>56</sup>  
796 e2pdb2mrc. For this last step, a resolution of 5 Å was chosen based on visual assessment of the  
797 EMAN2 outputs relative to those from ManifoldEM. Projections of these 20 MRCs were then  
798 taken using the standard projection operator in e2project3d with C1 symmetry in EMAN2.  
799 Importantly, the Euler coordinates for these projections were supplied by those representing the  
800 64 ManifoldEM anchors (after correcting for a coordinate transformation from ManifoldEM to  
801 ZXZ’ convention). Finally, these projections were combined into sequences for each PD to form  
802 64 20-frame 2D movies of the WE trajectory.

803

#### 804 **1.2.4 Comparison of WE simulations to ManifoldEM outputs**

805 As shown in **Supplementary Videos 2 and 3**, and described in detail within our main text, a  
806 striking visual resemblance emerged between conformational motions obtained by WE  
807 simulation and experiment. For heightened visual aid, 2D movies from the WE simulation and

808 the ManifoldEM corresponding to the same PD (and RC therein) were next overlaid to directly  
809 highlight similarities and differences. For this procedure, we first layered the ManifoldEM movie  
810 over a homogenous red backdrop and applied a Linear Dodge blend mode, with a similar effect  
811 applied on the WE movie over a blue backdrop (see **Supplemental Fig. 4** for the results of these  
812 operations). We next multiplied the ManifoldEM composite image and the WE composite image  
813 together. As an outcome of this multiplication, pixels that are white (signal) in both movies  
814 retain their whiteness in the composite. In this way, whiteness in the composite movie becomes a  
815 qualitative measure of similarity between conforming domains, while non-white regions  
816 emphasize differences.

817

818 Finally, this overlaying approach was used to estimate the total extent of the RBD motion as  
819 expressed in the ManifoldEM and WE frameworks. For this comparison, CC1 from a side view  
820 (PD 1386) was chosen based on its highly prominent view of RBD-“up” to RBD-“down”  
821 motion. Next, the ManifoldEM movie was time-remapped to align it optimally in time with the  
822 motions observed in the corresponding WE movie (**Supplementary Video 2**). Using the  
823 multiplication-composite as a guide, it was determined that the ManifoldEM RBD domain  
824 reaches its full extent in the “up” position at the 14<sup>th</sup> frame out of the 20 frames from the WE  
825 trajectory, before the WE trajectory moves onward to a more fully open state. With this  
826 knowledge, the total difference in conformational extents was estimated at 11 Å as calculated via  
827 RBD — core distance.

828

829

### 830 **1.3 Experimental Methods**

831

#### 832 *Protein Expression and Purification*

833 Substitutions N343A, D405A, R408A, and D427A were cloned into the HexaPro SARS-CoV-2  
834 spike background.<sup>23</sup> A spike variant with all RBDs locked in the “down” position through the  
835 introduction of a disulfide bond was similarly produced through cysteine substitutions at residues  
836 S383C and D985C in the HexaPro protein.<sup>25</sup> All variants were expressed through  
837 polyethyleneimine-induced transient transfection of FreeStyle 293-F cells (Thermo Fisher). After  
838 4 days, cell supernatant was clarified by centrifugation, passed through a 0.22 µm filter, and

839 purified over StrepTactin resin (IBA). Variants were further purified by size-exclusion  
840 chromatography on a Superose 6 10/300 column (GE Healthcare) in a buffer consisting of 2 mM  
841 Tris pH 8.0, 200 mM NaCl and 0.02% NaN<sub>3</sub>. Soluble ACE2 was produced and purified as  
842 previously described.<sup>8</sup>

843

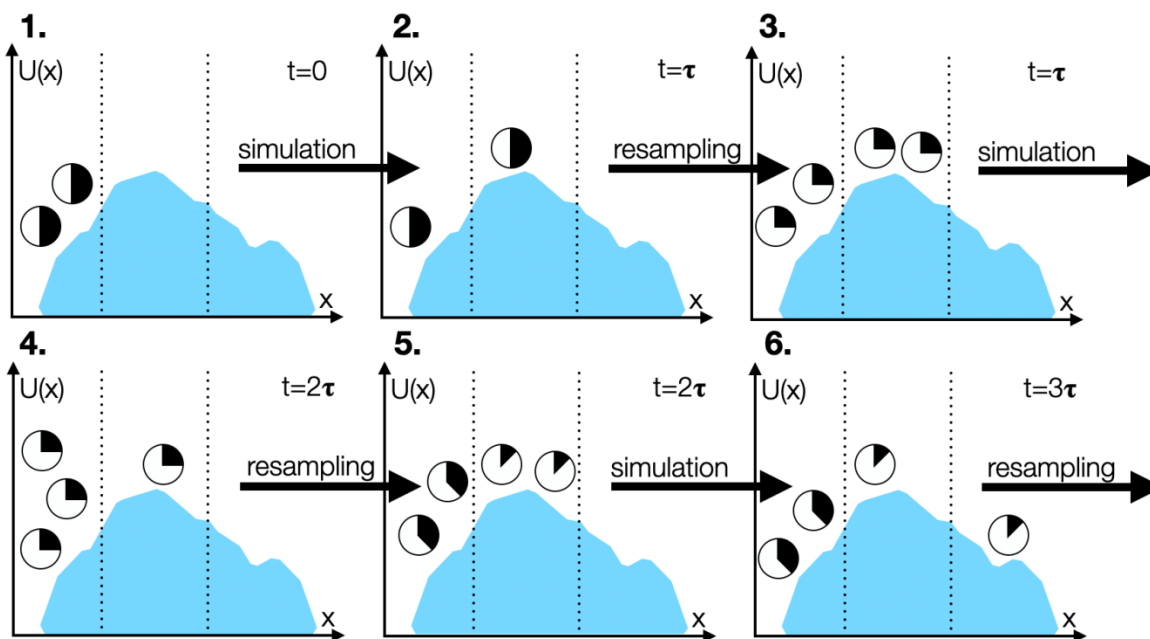
#### 844 *Biolayer Interferometry*

845 Anti-foldon IgG was immobilized to an anti-human Fc (AHC) Octet biosensor (FortéBio). Tips  
846 were then submerged into the specified HexaPro variants before being subsequently dipped into  
847 200 nM ACE2 to observe variant association, followed by dissociation in buffer consisting of 20  
848 mM Tris pH 7.5, 150 mM NaCl, 1 mg/mL bovine serum albumin, and 0.01% Tween-20. The  
849 relative proportion of RBD in an accessible state was quantified based on the binding level as  
850 previously described.<sup>8</sup> The S383C, D985C variant was used as a negative control. Data were  
851 collected in triplicate and replicate sensorgrams are shown in **Supplemental Fig. 16**.

852

853 2. Supplementary Figures

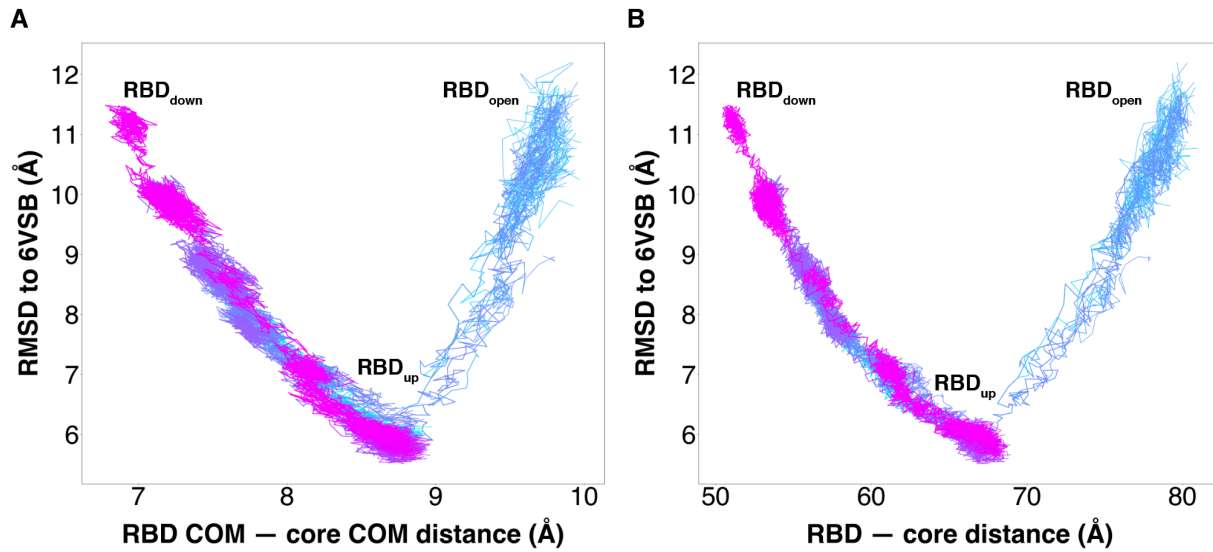
854



855

856 **Supplemental Fig. 1** Schematic of the weighted ensemble (WE) strategy. The WE strategy is  
 857 illustrated for a three-state system with a one-dimensional progress coordinate  $x$  that is divided  
 858 into bins.  $U(x)$  represents the potential of the system dependent on  $x$ , which can be seen from the  
 859 curve of the shaded region. 1. WE initiates two equally weighted trajectories (represented as  
 860 circles) from the first bin, each with a statistical weight of 0.5 (represented as filled parts of the  
 861 circles), for a fixed time interval  $\tau$ . 2. Resampling is then performed, replicating or terminating  
 862 trajectories to maintain a target number of two trajectories in each bin (e.g., in the first and  
 863 second bins, splitting the weight among the two child trajectories with a weight of 0.25 for each  
 864 trajectory). 3. Trajectories are run for another fixed time interval  $\tau$ . 4. After running, resampling  
 865 is performed (e.g., in the first bin, terminating two of the three trajectories and in the second bin,  
 866 replicating the one trajectory to yield two trajectories). 5. The system ends up with two  
 867 trajectories in each of the visited bins. 6. One of the trajectories ends up in the third bin. Rounds  
 868 of simulation and resampling are performed until a desired number of continuous pathways into  
 869 the target state are generated.

870

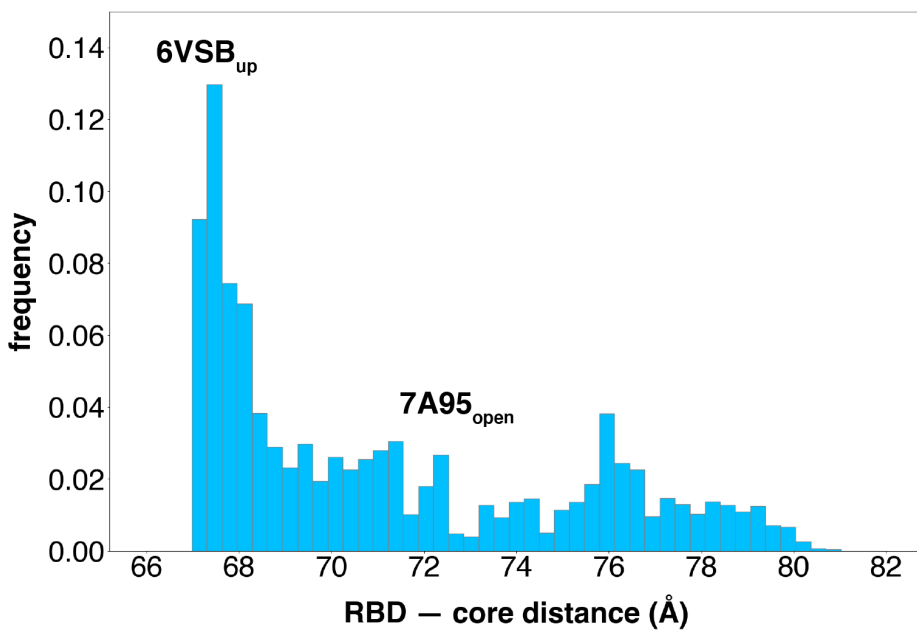


871  
 872 **Supplemental Fig. 2** Successful pathways of spike opening for the (A) actual and (B) intended  
 873 progress coordinate. Overlay of 310 successful pathways including 204 pathways of the RBD  
 874 transitioning from the “down” state to the “up” state (magenta-purple) and 106 pathways from  
 875 the “down” to the “open” states (purple to cyan). Continuous trajectories plotted with the  $C\alpha$   
 876 RMSD of the RBD to the 6VSB “up” state versus the RBD — core distance.  
 877



878

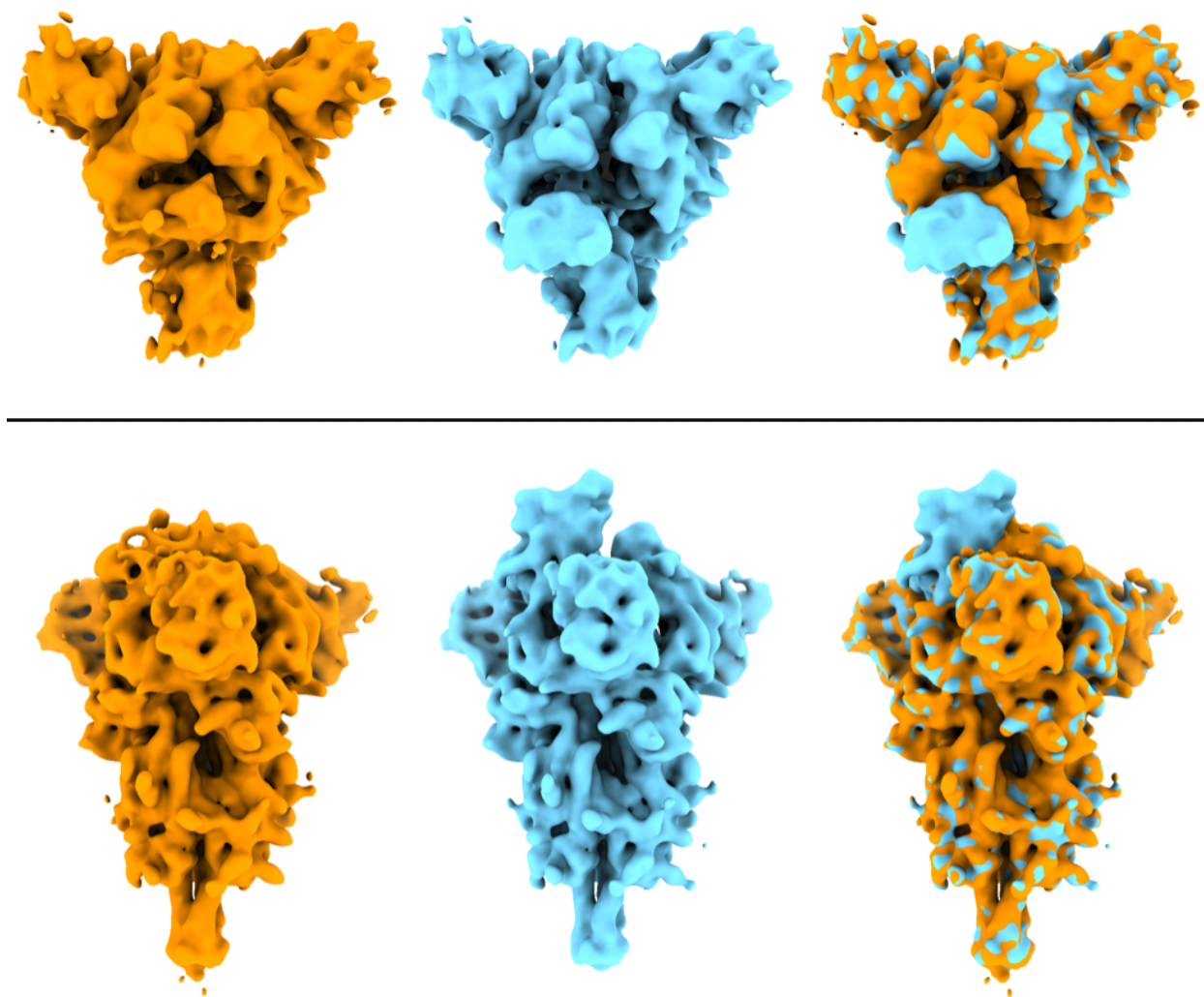
879



880

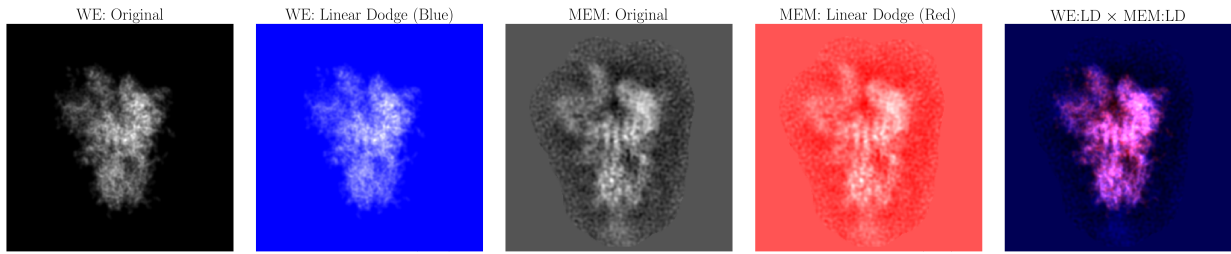
881 **Supplemental Fig. 3** Diversity of the simulated RBD “open” state ensemble. Probability  
882 distribution of RBD — core distances greater than the RBD “up” conformation defined by PDB  
883 6VSB (67.2 Å). The ACE2-bound structure from PDB 7A95 distance is 72.1 Å.

884

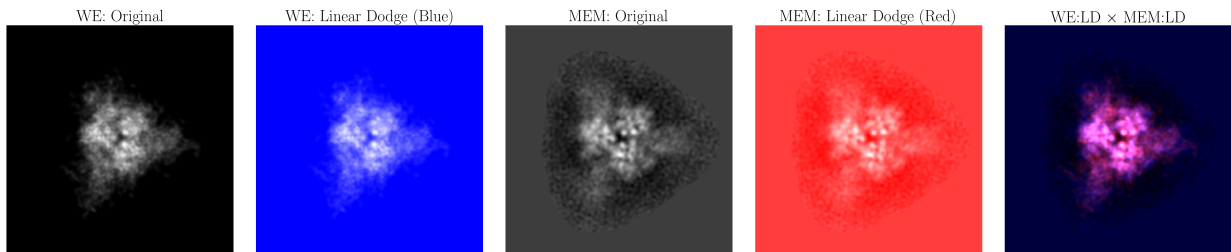


885  
886 **Supplemental Fig. 4** Comparison of two classes from the focused 3D classification in RELION  
887 with top and side views of the reconstructed classes. EM density maps are low pass filtered to 8  
888 Å for display purposes. The class with the RBD “down” conformation is displayed with orange  
889 on the left, the class with the RBD “up” is displayed with cyan in the center, and the  
890 superposition of both maps is shown on the right side to highlight their differences.  
891

PD 1386



PD 112



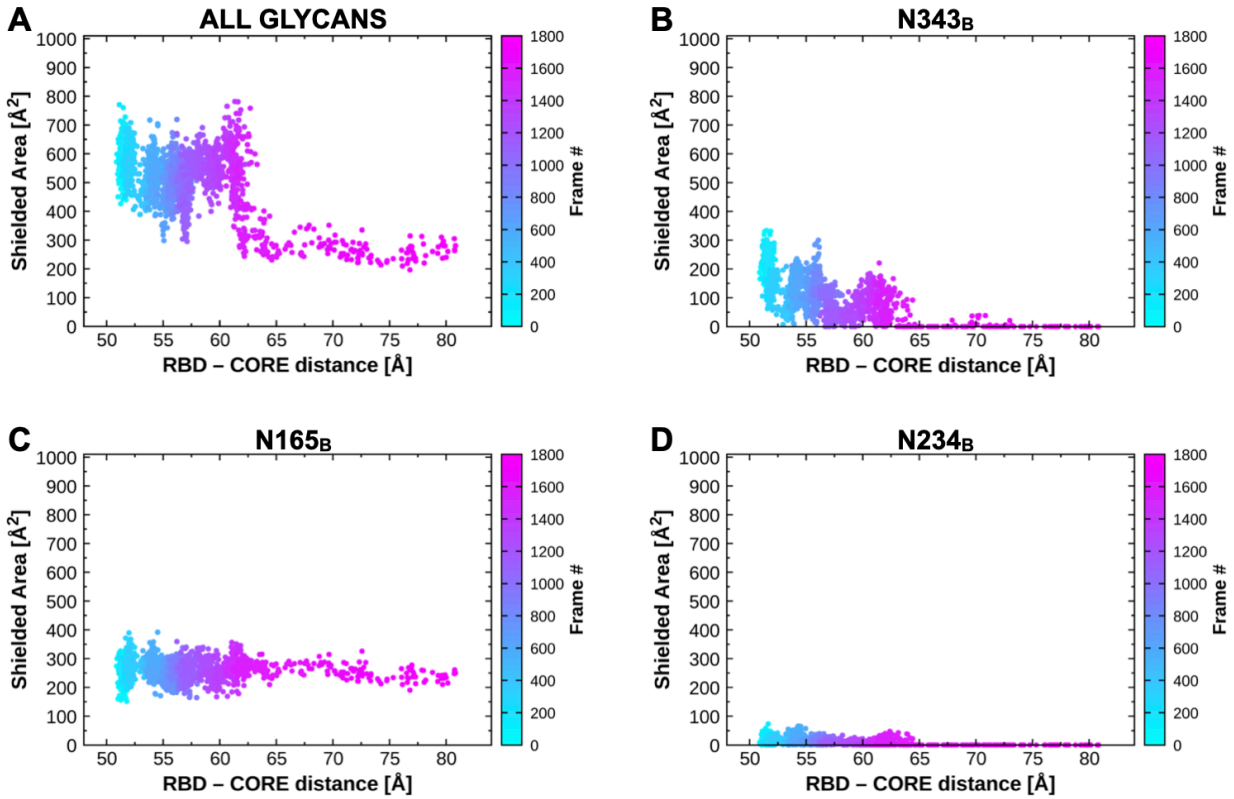
892

893 **Supplemental Fig. 5** Comparison of a frame from the WE and ManifoldEM (MEM) trajectory  
894 as seen from a side view (PD 1386) and top-down view (PD 112). For this comparison, image  
895 compositing techniques are applied on the outputs of each method as shown in the columns,  
896 including Linear Dodge and Multiply. As an example of its utility, after performing this  
897 operation on RC2 from a top-down view (PD 112), it can be seen that a collection of white pixels  
898 emerged in the composite movie (bottom-right entry), which strongly emphasize the similarities  
899 in positions of RBD and spike core helices between frameworks.

900

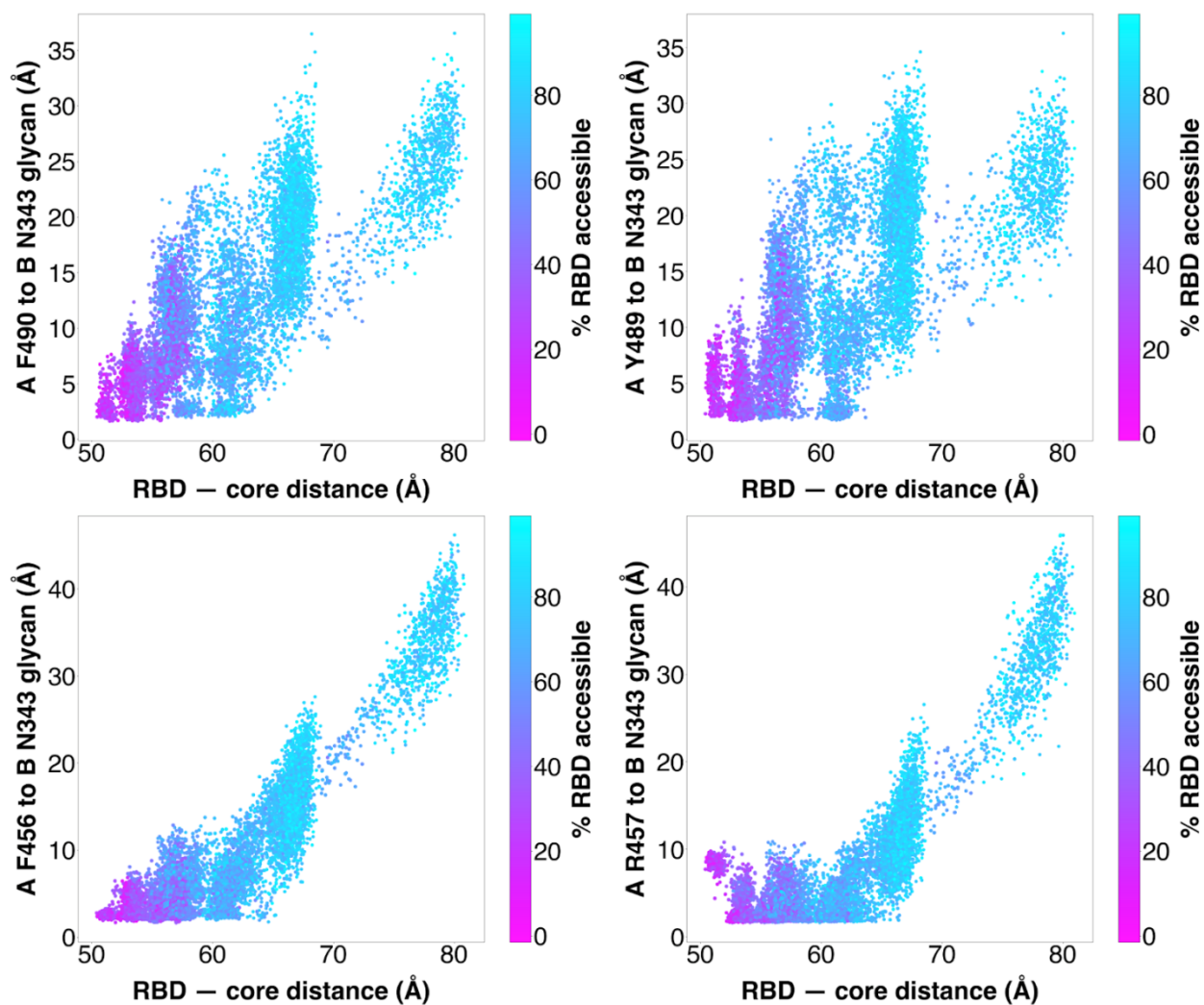
901

902



903  
 904 **Supplemental Fig. 6** Contribution of glycans shielding receptor binding motif along RBD  
 905 opening pathway. Shielded area represents the difference between the solvent accessible surface  
 906 area of the receptor binding motif in the presence and absence of (A) all three glycans, (B) N343,  
 907 (C) N165, or (D) N234.

908

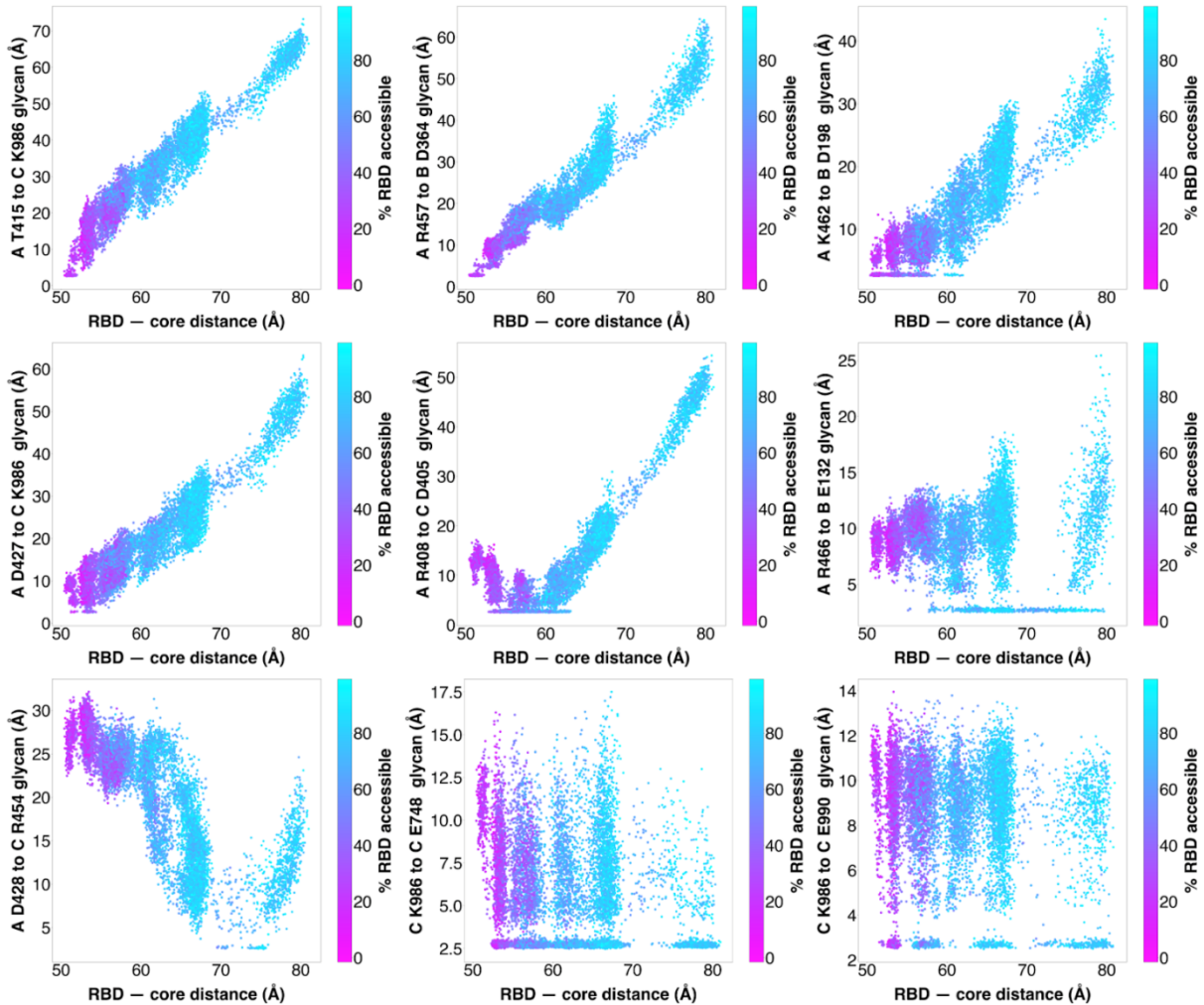


910

911 **Supplemental Fig. 7** Distance between N343 glycan and RBD residues. Scatter plot of data  
912 from the 310 continuous pathways with the minimum distance between the N343 glycan and  
913 RBD A residues F490, Y489, F456, or R457 plotted against RBD — core distance. Data points  
914 are colored based on % RBD solvent accessible surface area compared to the RBD “down” state  
915 6VXX.

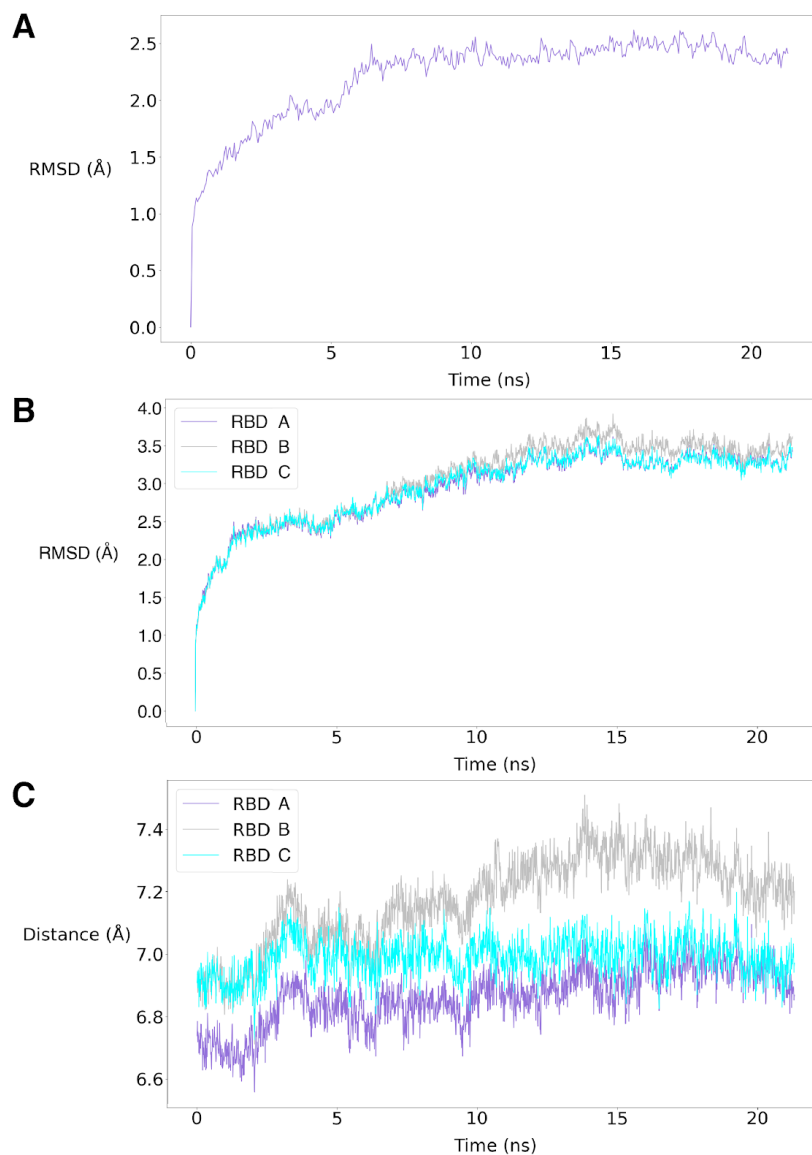
916

917  
918  
919



920  
921  
922  
923  
924  
925  
926

**Supplemental Fig. 8** Distance between salt-bridge and hydrogen bonding residues along the spike opening pathway. Scatter plot of data from the 310 continuous pathways with the minimum distance between the residues shown in **Figure 4** plotted against RBD-core distance. Data points are colored based on % RBD solvent accessible surface area compared to the RBD “down” state 6VXX.

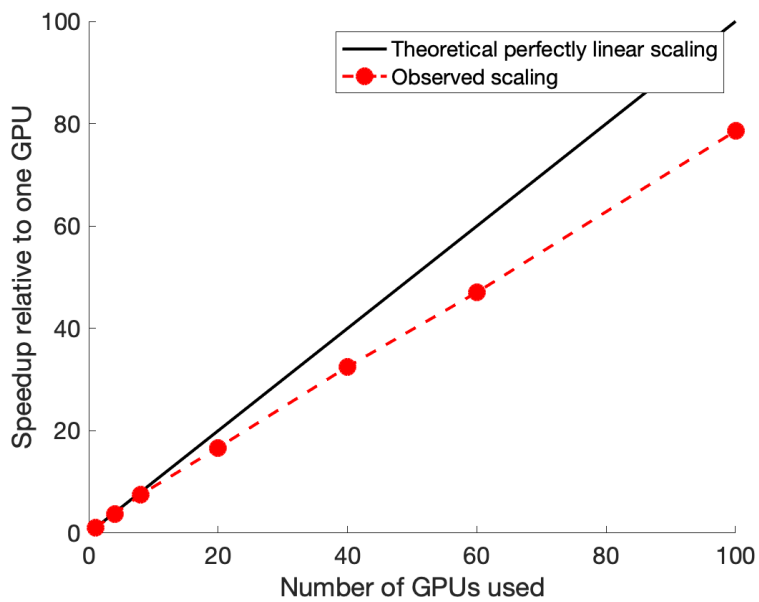


927

928 **Supplemental Fig. 9** Initial equilibration of a “down”-state structure using a standard MD  
 929 simulation. Time evolution of (A)  $C\alpha$  RMSD of protein residues , (B)  $C\alpha$  RMSD of structured  
 930 region of RBD after alignment of core domain to the initial structure and (C) Distance between  
 931 centers of mass of the RBD and core domain.

932

933



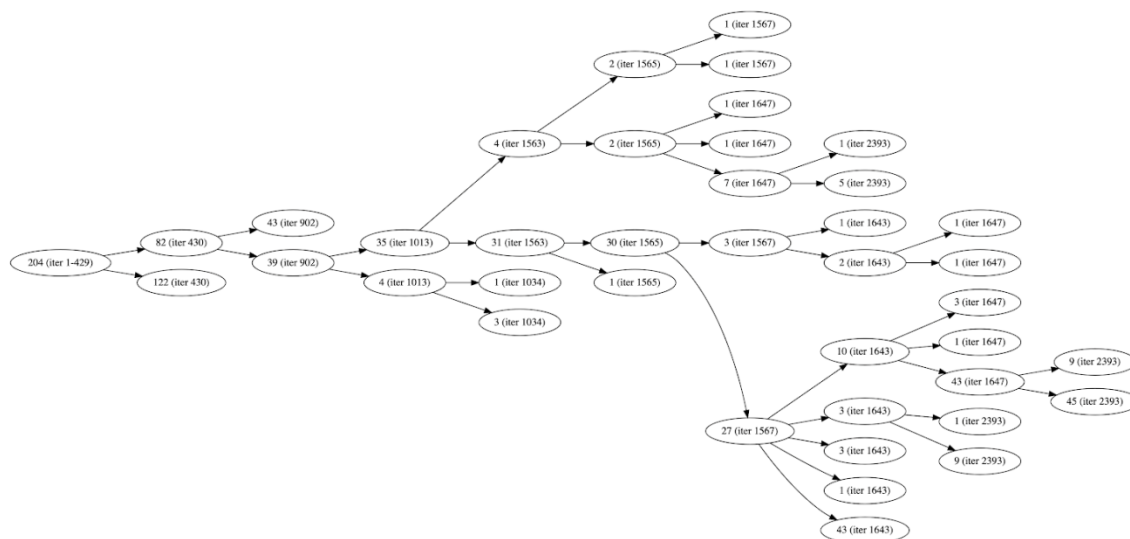
934

935 **Supplemental Fig. 10** Scaling of the WESTPA software using NVIDIA V100 GPUs on the  
936 TACC Longhorn supercomputer vs. theoretical perfectly linear scaling.

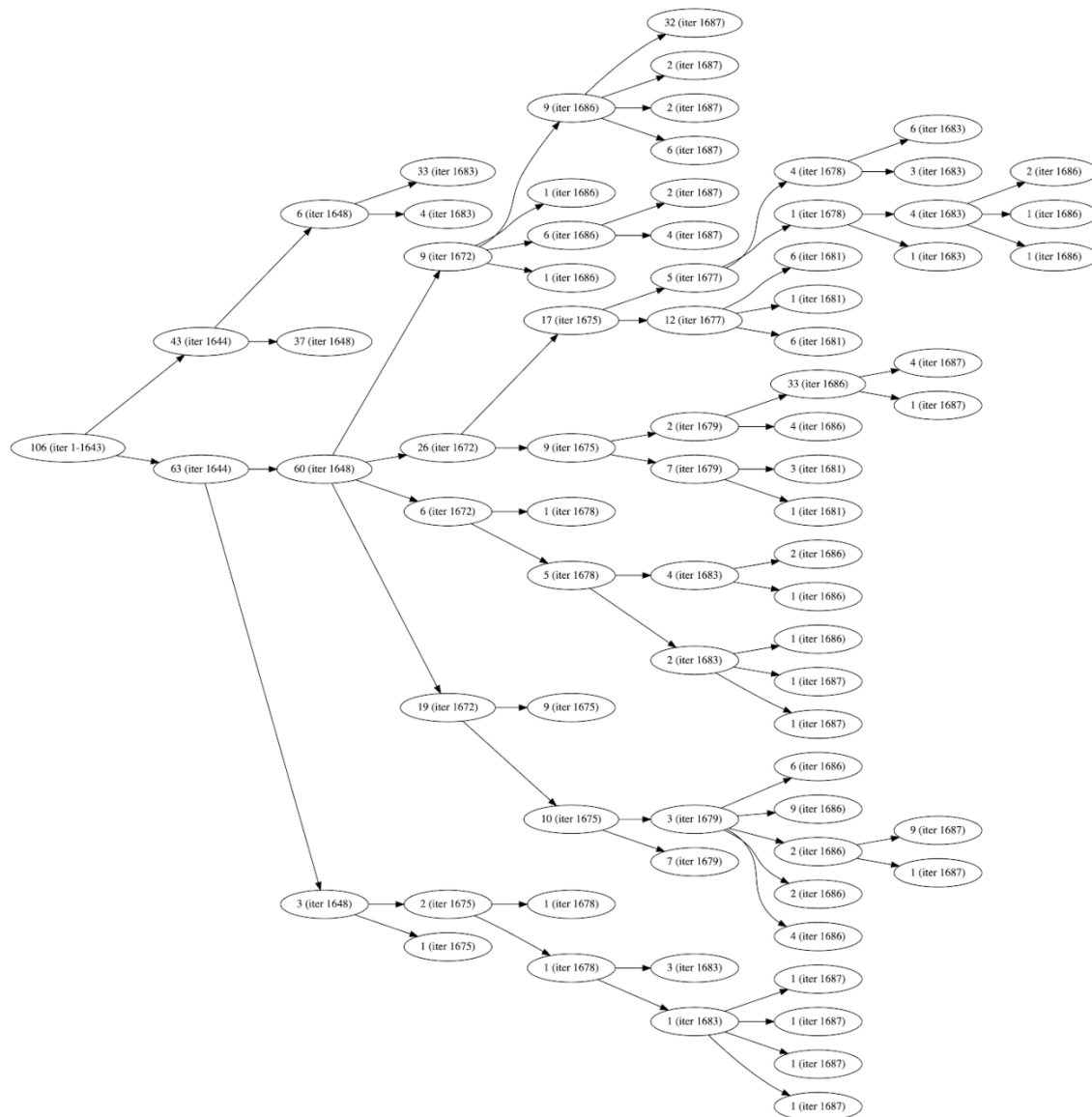
937



938  
939  
940



941  
942 **Supplemental Fig. 11** Trajectory splitting tree of the 204 independent pathways that reached the  
943 “up” state. The number of each node indicates the number of pathways at the given WE iteration  
944 in parentheses. All trajectories shared the same parents until iteration 429, with the first splitting  
945 of trajectories occurring at iteration 430. Subsequent splitting occurred at later iterations. Note  
946 that the sum of the child pathways does not necessarily match up with the parent’s number of  
947 pathways due to splitting and merging with other trajectories (not shown).



948

949 **Supplemental Fig. 12** Trajectory splitting tree of the 106 pathways that reached the “open”

950 state. The number of each node indicates the number of pathways at the given WE iteration in

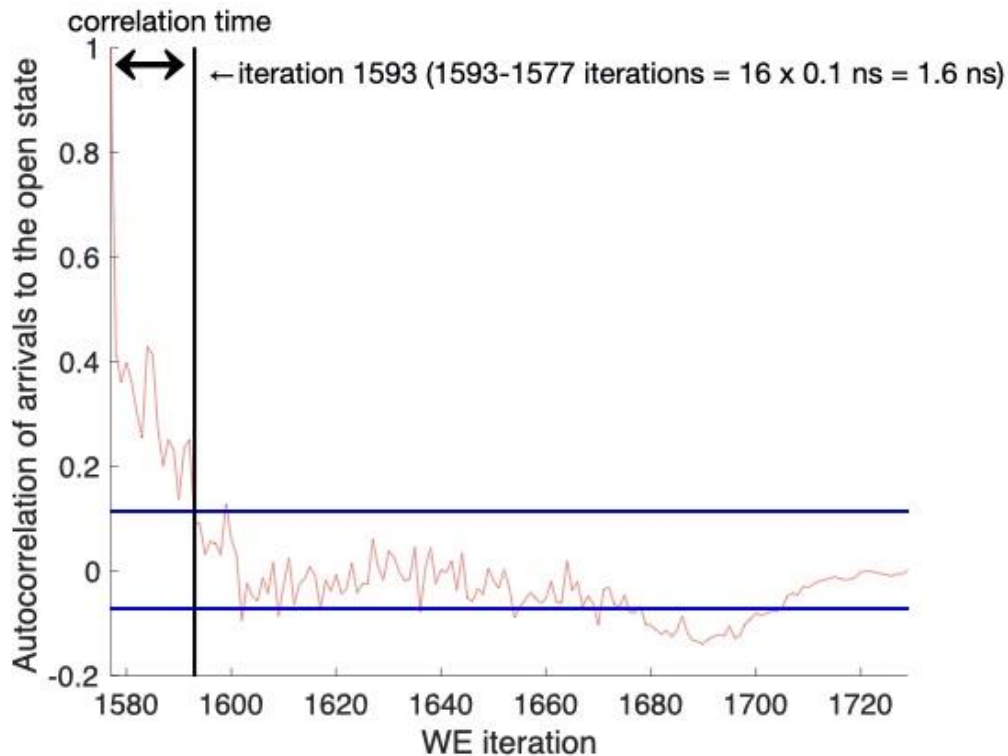
951 parentheses. All trajectories shared the same parents until iteration 1643, the first splitting of

952 trajectories occurring at iteration 1644. Note that the sum of the child pathways does not

953 necessarily match up with the parent’s number of pathways at subsequent iterations due to

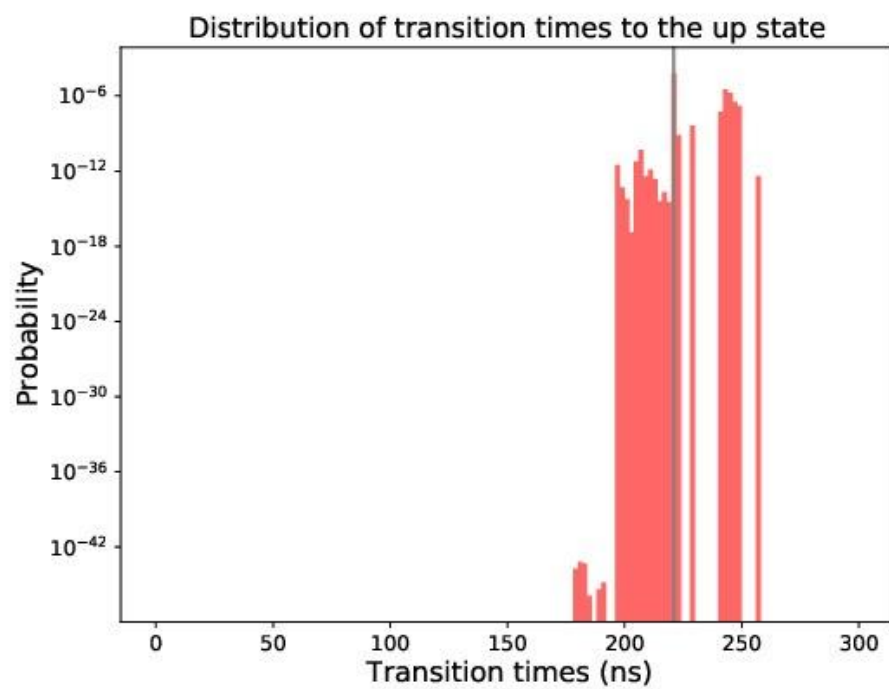
954 splitting and merging with other trajectories (not shown).

955



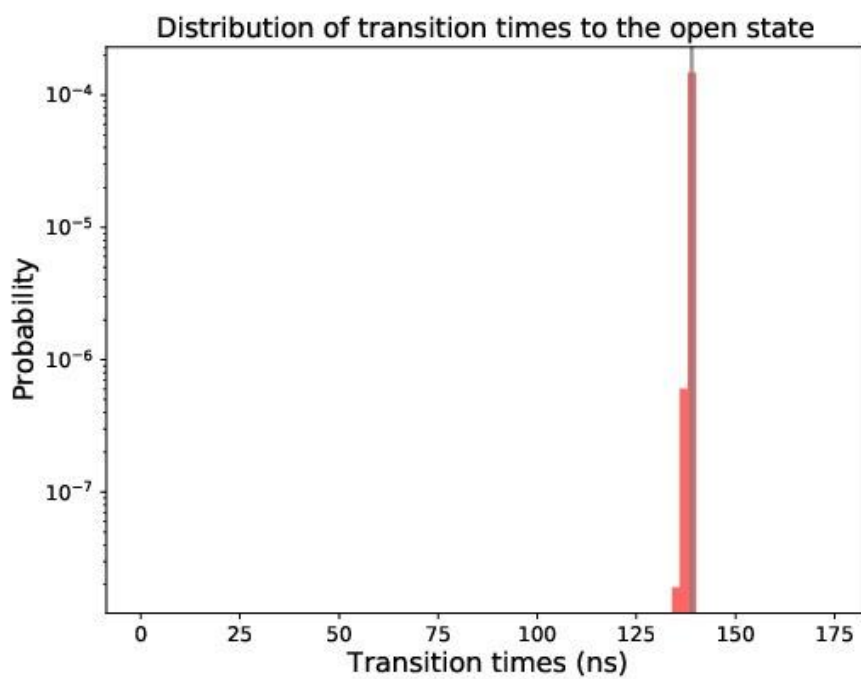
956  
 957  
 958  
 959  
 960  
 961  
 962  
 963

**Supplemental Fig. 13** Autocorrelation of arrivals from the “down” state to the “open” state (red) with a 95% confidence interval (blue). The confidence interval was generated using a Monte Carlo bootstrapping strategy where a bootstrap consisted of 1000 randomly drawn datasets (with replacement) from all “down”-to-“open” flux values. The vertical line marks the first point at which the autocorrelation falls within the confidence interval and is used to calculate the correlation time.

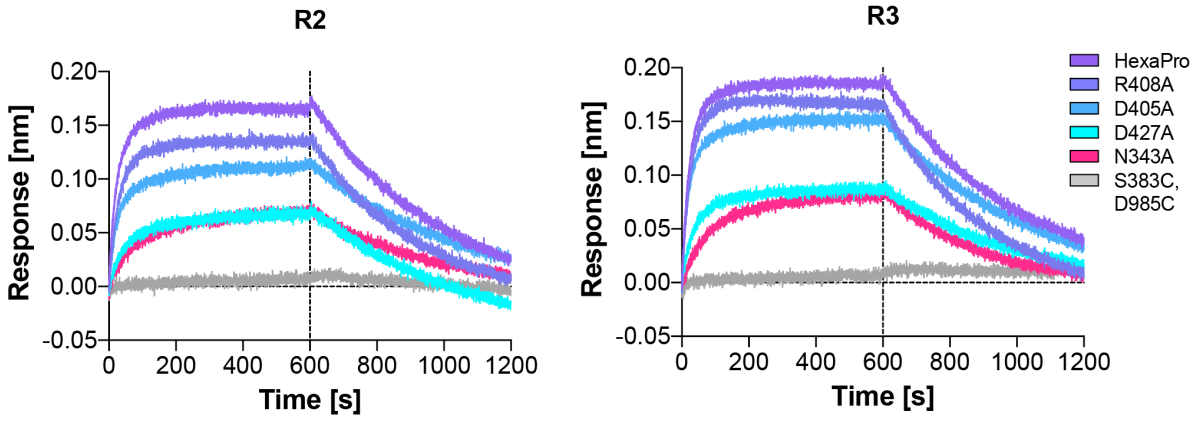


964  
965  
966  
967  
968

**Supplemental Fig. 14** Probability distribution of transition times from the “down” state to the “up” state. The most probable transition time is marked in grey. Note that the first 25% of the “fast” transitions are discarded here to calculate the most probable transition time.



969  
970 **Supplemental Fig. 15** Probability distribution of transition times from the “down” state to the  
971 “open” state. The most probable transition time is marked in grey. Note that the first 25% of the  
972 “fast” transitions are discarded here to calculate the most probable transition time.  
973



974  
 975  
 976  
 977

**Supplemental Fig. 16** BLI sensorgrams of spike variants binding to ACE2 from duplicate (R2) and triplicate (R3) experiments.

978 **3. Supplementary Tables**

979

980 **Supplemental Table 1** Biolayer interferometry data of spike variants binding to ACE2.

<b>VARIANT</b>	<b>HEXAPRO</b>	<b>R408A</b>	<b>D405A</b>	<b>D427A</b>	<b>N343A</b>
<b>R1 - Binding level (nm)</b>	0.1733	0.1560	0.1206	0.0913	0.0783
<b>R2 - Binding level (nm)</b>	0.1776	0.1467	0.1208	0.0793	0.0751
<b>R3 - Binding level (nm)</b>	0.1831	0.1629	0.1506	0.0849	0.0816
<b>Minimum (nm)</b>	0.1733	0.1467	0.1206	0.07932	0.07512
<b>Maximum (nm)</b>	0.1831	0.1629	0.1506	0.09131	0.0816
<b>Range (nm)</b>	0.0098	0.0162	0.03	0.01199	0.00648
<b>Mean (nm)</b>	0.1780	0.1552	0.1307	0.0852	0.0783
<b>Std. Deviation (± nm)</b>	0.0049	0.0081	0.0173	0.0060	0.0032
<b>Response (% to HexaPro)</b>	<b>100.00</b>	<b>87.19</b>	<b>73.43</b>	<b>47.85</b>	<b>44.01</b>
<b>Response decrease (%)</b>	<b>0.00</b>	<b>12.81</b>	<b>26.57</b>	<b>52.15</b>	<b>55.99</b>

981

982

983

984

985 **4. Supplementary Videos**

986 **Supplemental Video 1** Continuous pathway of RBD opening. This movie shows one of the  
987 continuous, unbiased pathways obtained from the WE simulations. All glycans are shown in blue  
988 except the N343 glycan which is colored magenta. Starting from all three RBDs in the “down”  
989 conformation, the chain A RBD lifts and twists counterclockwise into the “up” conformation,  
990 facilitated through interactions with the two adjacent RBDs, especially the N343 glycan gate on  
991 the chain B RBD. Upon reaching the “up” conformation, the RBD continues to twist into an  
992 “open” conformation en route to S1 dissociation.

993

994 **Supplemental Video 2** A comparison of the WE trajectory and ManifoldEM (MEM) CC1 and  
995 CC2 for a side view (PD 1386). It can be seen that there is strong agreement between the full WE  
996 trajectory and the sequential, piecewise combination of both CCs. Red arrows indicate direction  
997 of motion.

998

999 **Supplemental Video 3** A comparison of the WE trajectory and ManifoldEM (MEM) CC2 for a  
1000 top-down view (PD 112). A strong agreement can be seen between the outputs of these two  
1001 frameworks. To note, CC1 was not readily achievable from this view via manifold embedding,  
1002 since the RBD-“down” to RBD-“up” trajectory from this view is orthogonal to the plane of the  
1003 projection. Red arrows indicate direction of motion.

1004

1005 **Supplemental Video 4** Glycan gate at position N343 intercalates with residues to facilitate RBD  
1006 opening. This movie zooms in closer to the glycan at position N343 to show how RBD opening  
1007 is facilitated through intercalation between and underneath the residues F490, Y489, F456, F457  
1008 of RBD A. The glycan also transiently interacts with other residues of the RBD which are shown  
1009 when they are within Å from the glycan.

1010

1011 **Supplemental Video 5** Mapping of residue contacts to RBD throughout opening pathway.  
1012 Distances between residues throughout a continuous opening pathway calculated for the  
1013 trajectory shown in **Supplemental Videos 1 and 2**. Distances to each residue from RBD<sub>A</sub> are  
1014 shown for each chain in panels A-C and each of the glycans in panel D. Select regions are  
1015 labeled, and N165, N234, and N343 are labeled with +, ++, +++, respectively.

1016



1017 **4. Supplementary References**

1018

1019 (31) Huang, J.; MacKerell, A. D. CHARMM36 All-Atom Additive Protein Force Field:  
1020 Validation Based on Comparison to NMR Data. *J Comput Chem* **2013**, *34* (25), 2135–2145.  
1021 <https://doi.org/10.1002/jcc.23354>.

1022 (32) Guvench, O.; Hatcher, E. R.; Venable, R. M.; Pastor, R. W.; Mackerell, A. D. CHARMM  
1023 Additive All-Atom Force Field for Glycosidic Linkages between Hexopyranoses. *J Chem*  
1024 *Theory Comput* **2009**, *5* (9), 2353–2370. <https://doi.org/10.1021/ct900242e>.

1025 (33) Jorgensen, W. L.; Chandrasekhar, J.; Madura, J. D.; Impey, R. W.; Klein, M. L.  
1026 Comparison of Simple Potential Functions for Simulating Liquid Water. *J. Chem. Phys.*  
1027 **1983**, *79* (2), 926–935. <https://doi.org/10.1063/1.445869>.

1028 (34) Humphrey, W.; Dalke, A.; Schulten, K. VMD: Visual Molecular Dynamics. *J Mol Graph*  
1029 **1996**, *14* (1), 33–38, 27–28.

1030 (35) Götz, A. W.; Williamson, M. J.; Xu, D.; Poole, D.; Le Grand, S.; Walker, R. C. Routine  
1031 Microsecond Molecular Dynamics Simulations with AMBER on GPUs. 1. Generalized  
1032 Born. *Journal of Chemical Theory and Computation* **2012**, *8* (5), 1542–1555.  
1033 <https://doi.org/10.1021/ct200909j>.

1034 (36) Salomon-Ferrer, R.; Götz, A. W.; Poole, D.; Le Grand, S.; Walker, R. C. Routine  
1035 Microsecond Molecular Dynamics Simulations with AMBER on GPUs. 2. Explicit Solvent  
1036 Particle Mesh Ewald. *Journal of Chemical Theory and Computation* **2013**, *9* (9), 3878–  
1037 3888. <https://doi.org/10.1021/ct400314y>.

1038 (37) D.A. Case, I.Y. Ben-Shalom, S.R. Brozell, D.S. Cerutti, T.E. Cheatham, III, V.W.D.  
1039 Cruzeiro, T.A. Darden,; R.E. Duke, D. Ghoreishi, M.K. Gilson, H. Gohlke, A.W. Goetz, D.  
1040 Greene, R Harris, N. Homeyer, Y. Huang,; S. Izadi, A. Kovalenko, T. Kurtzman, T.S. Lee,  
1041 S. LeGrand, P. Li, C. Lin, J. Liu, T. Luchko, R. Luo, D.J.; Mermelstein, K.M. Merz, Y.  
1042 Miao, G. Monard, C. Nguyen, H. Nguyen, I. Omelyan, A. Onufriev, F. Pan, R.; Qi, D.R.  
1043 Roe, A. Roitberg, C. Sagui, S. Schott-Verdugo, J. Shen, C.L. Simmerling, J. Smith, R.  
1044 SalomonFerrer, J. Swails, R.C. Walker, J. Wang, H. Wei, R.M. Wolf, X. Wu, L. Xiao,  
1045 D.M. York and P.A. Kollman. AMBER 2018. *University of California, San Francisco.*  
1046 **2018.**

- 1047 (38) Lee, T.-S.; Cerutti, D. S.; Mermelstein, D.; Lin, C.; LeGrand, S.; Giese, T. J.; Roitberg, A.;  
1048 Case, D. A.; Walker, R. C.; York, D. M. GPU-Accelerated Molecular Dynamics and Free  
1049 Energy Methods in Amber18: Performance Enhancements and New Features. *J Chem Inf*  
1050 *Model* **2018**, *58* (10), 2043–2050. <https://doi.org/10.1021/acs.jcim.8b00462>.
- 1051 (39) Crowley, M. F.; Williamson, M. J.; Walker, R. C. CHAMBER: Comprehensive Support for  
1052 CHARMM Force Fields within the AMBER Software. *International Journal of Quantum*  
1053 *Chemistry* **2009**, *109* (15), 3767–3772. <https://doi.org/10.1002/qua.22372>.
- 1054 (40) Ryckaert, J.-P.; Ciccotti, G.; Berendsen, H. J. C. Numerical Integration of the Cartesian  
1055 Equations of Motion of a System with Constraints: Molecular Dynamics of n-Alkanes.  
1056 *Journal of Computational Physics* **1977**, *23* (3), 327–341. [https://doi.org/10.1016/0021-](https://doi.org/10.1016/0021-9991(77)90098-5)  
1057 [9991\(77\)90098-5](https://doi.org/10.1016/0021-9991(77)90098-5).
- 1058 (41) Darden, T.; York, D.; Pedersen, L. Particle Mesh Ewald: An N·log(N) Method for Ewald  
1059 Sums in Large Systems. *J. Chem. Phys.* **1993**, *98* (12), 10089–10092.  
1060 <https://doi.org/10.1063/1.464397>.
- 1061 (42) Zwier, M. C.; Adelman, J. L.; Kaus, J. W.; Pratt, A. J.; Wong, K. F.; Rego, N. B.; Suárez,  
1062 E.; Lettieri, S.; Wang, D. W.; Grabe, M.; Zuckerman, D. M.; Chong, L. T. WESTPA: An  
1063 Interoperable, Highly Scalable Software Package for Weighted Ensemble Simulation and  
1064 Analysis. *J. Chem. Theory Comput.* **2015**, *11* (2), 800–809.  
1065 <https://doi.org/10.1021/ct5010615>.
- 1066 (43) Roe, D. R.; Cheatham, T. E. PTRAJ and CPPTRAJ: Software for Processing and Analysis  
1067 of Molecular Dynamics Trajectory Data. *J. Chem. Theory Comput.* **2013**, *9* (7), 3084–3095.  
1068 <https://doi.org/10.1021/ct400341p>.
- 1069 (44) Hunter, J. D. Matplotlib: A 2D Graphics Environment. *Computing in Science Engineering*  
1070 **2007**, *9* (3), 90–95. <https://doi.org/10.1109/MCSE.2007.55>.
- 1071 (45) R. J. Gowers, M. Linke, J. Barnoud, T. J. E. Reddy, M. N. Melo, S. L. Seyler, D. L. Dotson,  
1072 J. Domanski, S. Buchoux, I. M. Kenney, and O. Beckstein. MDAnalysis: A Python  
1073 package for the rapid analysis of molecular dynamics simulations. In S. Benthall and S.  
1074 Rostrup, editors, *Proceedings of the 15th Python in Science Conference*. **2016**, 98-105.  
1075 Austin, TX, SciPy, doi:10.25080/majora-629e541a-00e.

- 1076 (46) N. Michaud-Agrawal, E. J. Denning, T. B. Woolf, and O. Beckstein. MDAnalysis: A  
1077 Toolkit for the Analysis of Molecular Dynamics Simulations. *J. Comput. Chem.* **2011**, 32  
1078 (10), 2319-2327. doi:10.1002/jcc.21787.
- 1079 (47) Decherchi, S.; Spitaleri, A.; Stone, J.; Rocchia, W. NanoShaper-VMD Interface:  
1080 Computing and Visualizing Surfaces, Pockets and Channels in Molecular Systems.  
1081 *Bioinformatics* **2019**, 35 (7), 1241–1243. <https://doi.org/10.1093/bioinformatics/bty761>.
- 1082 (48) Dashti, A.; Mashayekhi, G.; Shekhar, M.; Ben Hail, D.; Salah, S.; Schwander, P.; des  
1083 Georges, A.; Singharoy, A.; Frank, J.; Ourmazd, A. Retrieving Functional Pathways of  
1084 Biomolecules from Single-Particle Snapshots. *Nat. Commun.* **2020**, 11 (1), 1–14.  
1085 <https://doi.org/10.1038/s41467-020-18403-x>.
- 1086 (49) Scheres, S. H. W. RELION: Implementation of a Bayesian Approach to Cryo-EM Structure  
1087 Determination. *J. Struct. Biol.* **2012**, 180 (3), 519–530.  
1088 <https://doi.org/10.1016/j.jsb.2012.09.006>.
- 1089 (50) Punjani, A.; Rubinstein, J. L.; Fleet, D. J.; Brubaker, M. A. CryoSPARC: Algorithms for  
1090 Rapid Unsupervised Cryo-EM Structure Determination. *Nat. Methods* **2017**, 14 (3), 290–  
1091 296. <https://doi.org/10.1038/nmeth.4169>.
- 1092 (51) Punjani, A.; Fleet, D. J. 3D Variability Analysis: Resolving Continuous Flexibility and  
1093 Discrete Heterogeneity from Single Particle Cryo-EM. *J. Struct. Biol.* **2021**, 213 (2),  
1094 107702. <https://doi.org/10.1016/j.jsb.2021.107702>.
- 1095 (52) Coifman, R. R.; Lafon, S. Diffusion Maps. *Appl. Comput. Harmon. Anal.* **2006**, 21 (1), 5–  
1096 30. <https://doi.org/10.1016/j.acha.2006.04.006>.
- 1097 (53) Giannakis, D.; Majda, A. J. Nonlinear Laplacian Spectral Analysis for Time Series with  
1098 Intermittency and Low-Frequency Variability. *Proc. Natl. Acad. Sci. U. S. A.* **2012**, 109 (7),  
1099 2222–2227. <https://doi.org/10.1073/pnas.1118984109>.
- 1100 (54) Huang, C.C., Couch, G.S., Pettersen, E.F., and Ferrin, T.E. "Chimera: An Extensible  
1101 Molecular Modeling Application Constructed Using Standard Components." *Pacific*  
1102 *Symposium on Biocomputing* 1:724 (1996). <http://www.cgl.ucsf.edu/chimera>
- 1103 (55) Liebschner, D.; Afonine, P. V.; Baker, M. L.; Bunkoczi, G.; Chen, V. B.; Croll, T. I.;  
1104 Hintze, B.; Hung, L. W.; Jain, S.; McCoy, A. J.; Moriarty, N. W.; Oeffner, R. D.; Poon, B.  
1105 K.; Prisant, M. G.; Read, R. J.; Richardson, J. S.; Richardson, D. C.; Sammito, M. D.;  
1106 Sobolev, O. V.; Stockwell, D. H.; Terwilliger, T. C.; Urzhumtsev, A. G.; Videau, L. L.;

1107 Williams, C. J.; Adams, P. D. Macromolecular Structure Determination Using X-Rays,  
1108 Neutrons and Electrons: Recent Developments in Phenix. *Acta Crystallogr. Sect. D Struct.*  
1109 *Biol.* **2019**, 75 (Pt 10), 861–877. <https://doi.org/10.1107/S2059798319011471>.  
1110 (56) Tang, G.; Peng, L.; Baldwin, P. R.; Mann, D. S.; Jiang, W.; Rees, I.; Ludtke, S. J. EMAN2:  
1111 An Extensible Image Processing Suite for Electron Microscopy. *J. Struct. Biol.* **2007**, 157  
1112 (1), 38–46. <https://doi.org/10.1016/j.jsb.2006.05.009>.  
1113  
1114